Title

Membrane Cholesterol Enrichment of Red Blood Cell-Derived Microparticles Results in Prolonged Circulation.

Journal

ACS applied bio materials, 5(2)

ISSN

2576-6422

Authors

Tang, Jack C
Lee, Chi-Hua
Lu, Thompson
et al.

Publication Date

2022-02-01

DOI

10.1021/acsabm.1c01104

Peer reviewed

HHS Public Access

Author manuscript

ACS Appl Bio Mater. Author manuscript; available in PMC 2023 February 21.

Published in final edited form as:

ACS Appl Bio Mater. 2022 February 21; 5(2): 650–660. doi:10.1021/acsabm.1c01104.

Membrane Cholesterol Enrichment of Red Blood Cell-Derived Microparticles Results in Prolonged Circulation

Jack C. Tang,

Department of Bioengineering, University of California, Riverside, Riverside, California 92521, United States; Present Address: University of Southern California, Los Angeles, California 90033, United States

Chi-Hua Lee,

Department of Biochemistry, University of California, Riverside, Riverside, California 92521, United States

Thompson Lu,

Department of Bioengineering, University of California, Riverside, Riverside, California 92521, United States

Raviraj Vankayala,

Department of Bioengineering, University of California, Riverside, Riverside, California 92521, United States; Present Address: Indian Institute of Technology Jodhpur, Karwar, Jodhpur, Rajasthan 342037, India

Taylor Hanley,

Department of Bioengineering, University of California, Riverside, Riverside, California 92521, United States

Chiemerie Azubuogu,

Department of Bioengineering, University of California, San Diego, La Jolla, California 92023, United States

Jiang Li,

Corresponding Author: **Bahman Anvari** – *Department of Bioengineering and Department of Biochemistry, University of California, Riverside, Riverside, California 92521, United States*; anvarib@ucr.edu.

Author Contributions

J.C.T. and C.-H.L. contributed equally to this work. The manuscript was written through contributions of all authors. B.A. conceived the project; contributed to the design of the experiments and interpretation of results; guided the presentation of figures; revised the manuscript; and supervised the project. J.C.T. and C.-H.L. contributed to the design of the experiment and interpretation of results; carried out the experiments; prepared the figures; and drafted the manuscript. T.L. obtained the QPI results. R.V., T.H., and C.A. assisted with experiments. J.L. and M.G.N. helped in obtaining the flow cytometry measurements using the LSR II flow cytometer. W.J. contributed to the design of the experiments. All authors have given approval to the final version of the manuscript.

Complete contact information is available at: https://pubs.acs.org/10.1021/acsabm.1c01104

Supporting Information

The Supporting Information is available free of charge at https://pubs.acs.org/doi/10.1021/acsabm.1c01104.

Quantification of cholesterol content and summary of in vivo results (PDF)

The authors declare the following competing financial interest(s): Author B.A. has a financial interest in Radoptics LLC, which is pursuing the commercial development of the particles reported in this manuscript. This interest did not interfere with the scientific work, judgment, and objectivity of the investigators in regard to the experimental procedures, analyses, and reporting and interpretation of results, or any other aspect of the study. All the remaining authors declare that they have no conflict of interests. This information is also noted in the manuscript.

Division of Biomedical Sciences, University of California, Riverside, Riverside, California 92521, United States

Meera G. Nair,
Division of Biomedical Sciences, University of California, Riverside, Riverside, California 92521, United States

Wangcun Jia,
Beckman Laser Institute & Medical Clinic, University of California, Irvine, Irvine, California 92617, United States

Bahman Anvari
Department of Bioengineering and Department of Biochemistry, University of California, Riverside, Riverside, California 92521, United States

Abstract

Particles fabricated from red blood cells (RBCs) can serve as vehicles for delivery of various biomedical cargos. Flipping of phosphatidylserine (PS) from the inner to the outer membrane leaflet normally occurs during the fabrication of such particles. PS externalization is a signal for phagocytic removal of the particles from circulation. Herein, we demonstrate that membrane cholesterol enrichment can mitigate the outward display of PS on microparticles engineered from RBCs. Our in-vitro results show that the phagocytic uptake of cholesterol-enriched particles by murine macrophages takes place at a lowered rate, resulting in reduced uptake as compared to RBC-derived particles without cholesterol enrichment. When administered via tail-vein injection into healthy mice, the percent of injected dose (ID) per gram of extracted blood for cholesterol-enriched particles was ~1.5 and 1.8 times higher than the particles without cholesterol enrichment at 4 and 24 h, respectively. At 24 h, ~43% ID/g of the particles without cholesterol enrichment was eliminated or metabolized while ~94% ID/g of the cholesterol-enriched particles were still retained in the body. These results indicate that membrane cholesterol enrichment is an effective method to reduce PS externalization on the surface of RBC-derived particles and increase their longevity in circulation.

Graphical Abstract

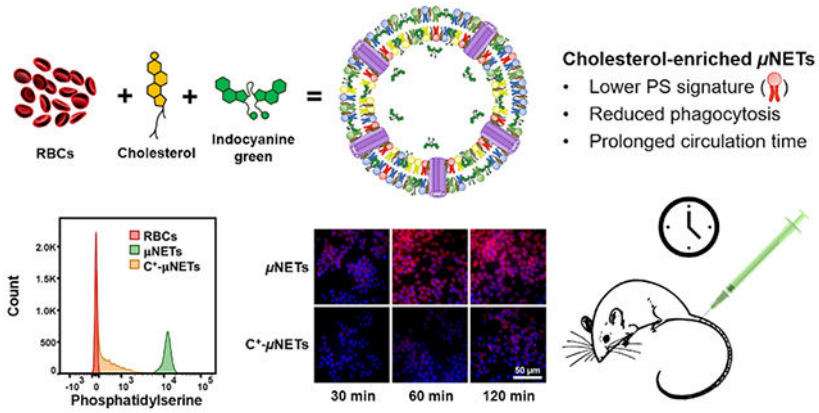

Keywords

biological vectors; biomimetics; drug delivery; erythrocytes; indocyanine green

INTRODUCTION

Particles fabricated from red blood cells (RBCs) provide a platform for the delivery of a variety of biomedical cargos,[1] including chemotherapeutic drugs,[2–4] photosensitizers,[3–5] and imaging contrast agents.[4,6–9] A key principle motivating the use of RBCs as delivery vehicles is the presence of specific membrane proteins including CD47, which prevents phagocytic uptake by macrophages, and CD55 and CD59, which protect the RBCs from complement damage and cell lysis.[10] These membrane proteins offer a mechanism for a prolonged circulation time of the cargo before the vehicles are ultimately eliminated by the immune system.

Common methods for encapsulation of various cargos into RBC-based platforms are based on biochemical treatment of RBCs in hypotonic buffers or by exposure of RBCs to electric field pulses (i.e., electroporation).[11–16] Phospholipids in the membrane bilayer of RBCs and other eukaryotic cells have an asymmetrical distribution where phosphatidylserine (PS) and phosphatidylethanolamine are confined to the inner (cytosolic facing) leaflet and phosphatidylcholine and sphingomyelin are predominantly in the outer (extracellular facing) leaflet.[17–19] Hypotonic treatment and electroporation can result in flipping of PS from the inner to the outer leaflet.[20–25] Physiologically, flipping of PS is associated with RBC senescence, where it serves as an “eat-me” signal for phagocytosis by splenic macrophages that contain a PS receptor.[26,27]

Transmembrane amino-phospholipid translocases (flippases) are involved in localization of PS by actively transferring it from the outer to the inner leaflet of the membrane in an ATP-dependent manner, with ATP11C identified as a major flippase in human RBCs.[28] In addition to flippases, transmembrane scramblases bidirectionally and nonselectively transport phospholipids in a Ca^{2+}-dependent but ATP-independent manner, with phospholipid scramblase 1 (PLSCR1) considered as a key scramblase in human RBCs.[19,28,29]

It has been reported that cholesterol is an important regulator of PLSCR1 activity and PS localization to the inner leaflet of the membrane.[28] Specifically, decreasing the cholesterol content of RBCs has been shown to activate PS scrambling and externalization of PS to the outer membrane leaflet. van Zwieten et al. have also reported that cholesterol depletion led to increased PS flipping.[30] The exact mechanism for cholesterol-induced inhibition of PLSCR1 remains to be elucidated, but it is thought to involve a cholesterol-binding motif in PLSCR1.[31]

In relation to microparticle delivery systems derived from RBCs, the inhibitory effects of cholesterol on PS flipping and the subsequent phagocytic outcomes have not been studied. Herein, we demonstrate for the first time that enrichment of the membrane cholesterol of microparticles fabricated from RBCs can be used to reduce PS externalization to the outer

leaflet of these particles and, subsequently, decrease the uptake of the particles by murine model macrophages in vitro and increase the circulation time concomitant with lowered distributions in the reticuloendothelial system (RES) of mice.

In this study, we have used indocyanine green (ICG), a near-infrared (NIR) sensitive molecule, approved by the FDA for specific clinical indications[32–34] and with extensive utility in clinical fluorescence imaging[35–39] as the cargo of choice for encapsulation. Additionally, ICG serves as an optical marker for quantitative assessment of the biodistribution of RBC-derived particles. We refer to these particles as microsized NIR erythrocyte-derived transducers (μNETs) as they can transduce NIR light to emit fluorescence, generate heat, or produce reactive oxygen species.[5,20] We have previously investigated the use of μNETs for real-time intravascular fluorescence imaging and photothermal destruction of the microvasculature, similar to vascular malformations found in port wine stain lesions.[20] ICG-doped RBCs have been used to characterize microvascular vasomotion in humans.[15,16] We have used nanosized RBC-derived particles containing ICG for NIR fluorescence imaging and photodestruction of tumors in animal models.[5,40] The present study is an important step towards the engineering of RBC-derived particles with appropriate biochemical characteristics, based on cholesterol incorporation, to enhance the bioavailability of the particles resulting from reduced clearance by the immune cells. Membrane cholesterol enrichment is also relevant to the fabrication of RBC-based particles containing not only optical materials but also other types of biomedical cargos.[41,42]

MATERIALS AND METHODS

Fabrication of μNETs and μNETs with Cholesterol-Enriched Membranes.

RBCs were isolated from 1 mL of whole human blood (Biological Specialty Corp.) by centrifugation twice in cold (4 °C) isotonic (~300 mOsm) phosphate-buffered saline (PBS) (referenced as 1× PBS). Isolated RBCs were then repeatedly washed in 1 mL of cold hypotonic PBS (0.25×, 15 min, 20,000*g*) to deplete the hemoglobin content of the cells. The resulting microsized erythrocyte ghosts (μEGs) were resuspended in 1 mL of 1× PBS. We designate the μEGs in 1 mL of solution as having a relative number concentration of 1 N.

To load ICG (MP Biochemicals) into μEGs, we added 1 mL of 300 μM ICG dissolved in water into the solution consisting of 1 mL of 1 N μEGs and 1 mL of 0.1 M Sørensen's buffer (Na_2HPO_4/NaH_2PO_4, ~140 mOsm, pH ~ 8), resulting in an ICG concentration of 100 μM in this loading buffer (~147 mOsm). To form μNETs, μEGs were incubated in this solution for 30 min at 4 °C (Figure 1). The resulting μNETs were then washed twice in 1 mL of 1× PBS (15 min, 20,000*g*) and resuspended in 4 °C 1× PBS to a final volume of 1 mL and stored at 4 °C for no longer than 24 h before experiments.

Methyl-β-cyclodextrin (MβCD) is commonly used to generate cholesterol inclusion complexes that donate cholesterol to the membrane of cells.[43,44] To form βNETs with enriched membrane cholesterol (referred to as C^+-μNETs), isolated RBCs were incubated in hypotonic 0.25× PBS solution containing the cholesterol–MβCD complex (48 mg of cholesterol per gram of cholesterol–MβCD complex) (Sigma-Aldrich), followed by centrifugation (15 min, 20,000*g*, 4 °C) (Figure 1). In this study, the cholesterol concentration

within the cholesterol–MβCD complex was 15 mM because we determined that this particular concentration resulted in the maximum level of cholesterol being imparted to the membrane of μEGs as compared to other concentrations experimented in the range of 5–30 mM (Figure S1). For all cholesterol-loading procedures, the molar ratio of MβCD to cholesterol in the complex was ~5.8:1. The supernatant, containing hemoglobin and excess cholesterol–MβCD complex, was decanted, and 1 mL of fresh 0.25× PBS solution containing the cholesterol–MβCD complex was added. This process was repeated until the supernatant became colorless. The pellet, consisting of cholesterol-enriched μEGs, was then loaded with ICG using the same method described above to form C^+-μNETs. To account for slight differences in the loading efficiency[45] of ICG into μNETs (~37%) and C^+-μNETs (~33%), we concentrated the suspension of C^+-μNETs accordingly so that both μNET and C^+-μNET solutions had the same absorbance value at 780 nm.

Characterization of Particles.

We measured the ζ potentials (Zetasizer Nano series, NanoZS90, Malvern Instruments) of the particles suspended in 1× PBS using folded capillary ζ cells. Five individual measurements were collected for each sample and averaged to determine the mean ζ potential ± standard deviation (SD). Absorption spectra of μNETs and C^+-μNETs suspended in 1× PBS were recorded in the spectral range of 280 to 900 nm using a UV—visible spectrophotometer (jasco V-670 UV—vis spectrophotometer, JASCO) with an optical path length of 1 cm. Fluorescence spectra of μNETs and C^+-μNETs suspended in 1× PBS in response to photoexcitation at 780 ± 2.5 nm filtered from a 450 W xenon lamp were obtained using a fluorometer (Fluorolog-3 spectrofluorometer, Edison). Normalized fluorescence emission $\chi(\lambda)$ spectra were quantified as

$$\chi^{(\lambda)} = \frac{F(\lambda)}{1 - 10^{-A(\lambda_{ex})}} \quad (1)$$

where F is the fluorescence emission intensity in response to the excitation wavelength (λ_{ex}) and $A(\lambda_{ex})$ is the absorbance of the sample at the excitation wavelength. Each NET solution was diluted 10-fold in 1× PBS prior to absorption and fluorescence measurements.

We imaged the RBCs, μNETs, and C^+-μNETs by a quantitative phase imaging (QPI) system and used the images to estimate their mean Feret diameters. Any abnormally shaped RBCs or particles (e.g., nondiscoidal shapes in RBCs or noncircular μNETs/C^+μNETs) were excluded from the analysis. Details of the QPI system are described in previous publications.[46,47] Briefly, samples were illuminated by a 100 W halogen lamp source through a condenser annulus and condenser lens. A 100× oil immersion objective (NA = 1.3) was used to collect the scattered and unscattered components of light passing through the sample. The light after sample illumination was filtered to a center wavelength of 595 ± 30 nm prior to exiting the microscope. A mirror directed the scattered and unscattered light to a linear polarizer. The unscattered light formed an image of the condenser annulus on a reflective spatial light modulator (SLM) (Hamamatsu LCOS-SLM X-10468). The SLM was used to introduce four phase shifts in π/2 increments to the unscattered light. The unscattered components interfered with the scattered light to form an image of the

sample, which was focused onto an electron-multiplying charge-coupled device (C9100-13, Hamamatsu). To accommodate full rearrangement of the nematic liquid crystals in the SLM, field delays of 100 ms were used between the phase modulations. We acquired 10 phase-shifted images every second to yield quantitative phase images at 2.5 frames per second. We designate the image intensity at a given pixel location *i, j* resulting from the interference between the scattered light and unscattered light at four different phase modulations as I_0, I_π, $I_{\pi/2}$, and $I_{(3\pi)/2}$ respectively. Values of the phase difference ($\Delta\varphi$) associated with each interference signal intensity are given as

$$\Delta\varphi(i,j) = \tan^{-1}\left(\frac{I_{3\pi/2} - I_{\pi/2}}{I_\pi - I_0}\right) \tag{2}$$

We subsequently obtained the resulting phase maps as

$$\varphi(i,j) = \tan^{-1}\left(\frac{\beta \sin \Delta\varphi}{1 + \beta \cos \Delta\varphi}\right) \tag{3}$$

where β is the ratio of the amplitude of scattered to unscattered light intensity at a given pixel location.

We have previously carried out extensive characterizations of RBC-derived optical microparticles doped with ICG.[45,48–50] These studies include ICG concentration-dependent characterizations of the ζ potential, absorption and emission spectra, excitation–emission maps, relative fluorescence quantum yield, and quantification of optical stability and ICG leakage dynamics and are not repeated here as they are not the subject of this particular study.

Cholesterol Quantification Assay.

We quantified the membrane cholesterol content in RBCs (positive control), μNETs (negative control), and C^+-μNETs using the Amplex Red Cholesterol Assay Kit (invitrogen Molecular Probes). We performed the assay by following the manufacturer's instructions using a 96-well plate (Corning, Inc.). Briefly, we oxidized the membrane-bound cholesterol using cholesterol oxidase to yield H_2O_2, which was then detected using the Amplex Red reagent (10-acetyl-3,7-dihydroxyphenoxazine) in the presence of horseradish peroxidase. Cholesterol oxidase contains a flavin adenine dinucleotide cofactor, which catalyzes the oxidation of cholesterol with O_2.[51] The reaction between the Amplex Red reagent and H_2O_2 produces resorufin, a highly fluorescent compound with respective absorption/emission maxima at 571 nm/585 nm in 50 mM sodium phosphate buffer (pH 7.4). We photoexcited the resorufin at 560 ± 2.0 nm, spectrally filtered from a xenon flash lamp, and obtained the emission recorded at 590 nm using a microplate reader (SpectraMax M3 microplate reader). We then compared the emission values to a cholesterol standard curve that related the fluorescence emission at the same wavelength to various concentrations of cholesterol in the reaction buffer, allowing us to quantify the amount of cholesterol in each sample.

Flow Cytometric Quantification of Externalized PS on Particles.

We used annexin V-Alexa Fluor 488 conjugate (AV-AF488) (Thermo Fisher Scientific) as a detection reagent to assay for PS externalization in μNETs and C^+-μNETs.[52,53] Specifically, we added 0.5 μL of each sample to 500 μL of annexin binding buffer (10 mM HEPES, 140 mM NaCl, and 2.5 mM $CaCl_2$ dissolved in water) and 40 μL of AV-AF488 and incubated them for ~20 min at 22 °C before analyzing them by flow cytometry (LSR II, BD Biosciences).

Our flow cytometric analysis of externalized PS on each sample was based on ICG fluorescence gating using the APC-Cy7 channel (633 nm excitation laser, 780 ± 30 nm emission filter). Out of the available excitation lasers and emission filters used in this flow cytometer instrument, these optical parameters yielded maximal NIR fluorescence from the ICG-loaded particle variants. We considered all ICG-positive events to result from the presence of either μNETs or C^+-μNETs. We determined the change in median fluorescence intensity (ΔMFI) of the AF488-labeled samples using the FITC/Alexa 488 channel of the LSR II (excitation wavelength = 488 ± 2 nm, fluorescence emission filter = 530 ± 15 nm) and additionally obtained forward scattering area (FSC-A) versus side scattering area (SSC-A) plots.

In-Vitro Assessment of Particle Uptake by RAW 264.7 Macrophages.

We used RAW 264.7 murine macrophages, stable at passage 11, to assess the uptake dynamics of μNETs and C^+- μNETs.[54] Cells were seeded at a density of ~100,000 per well in a 96-well tissue culture plate and incubated in 100 μL of Dulbecco's modified Eagle's medium (DMEM) supplemented with 10% fetal bovine serum and 1% penicillin/streptomycin for 24 h at 37 °C in 5% CO_2. To assess the uptake of each particle type, serum-supplemented DMEM in each well was removed, followed by adding 50 μL of 1 N sample mixed with 50 μL of serum-free DMEM to each well. Cells were incubated with each particle type at 37 °C with 5% CO_2 for 30, 60, and 120 min. At each time point, the particles were removed by washing the cells with 1× PBS. The cells were then fixed with 4% paraformaldehyde for 5 min, permeabilized with 2% Tween 20 for 5 min, and stained with 300 nM 4′,6-diamidino-2-phenylindole (DAPI) for 5 min. Between each of these steps, the cells were rinsed with 100 μL of sterile 1× PBS and finally rinsed twice more with 100 μL 1× PBS prior to fluorescence microscopy imaging using an inverted microscope (Eclipse Ti, Nikon).

We used a NIR filter set containing 740 ± 18 nm for photoexcitation and a long-pass filter (>780 nm) (41037—Li-Cor IR800, Chroma Technology Corp.) to capture the emitted fluorescence light. Cells' nuclei were visualized using a DAPI filter set (DAPI-5060B-NTE, Semrock Inc.) with 377 ± 25 nm for photoexcitation and 447 ± 30 nm for emission. ImageJ was used to normalize the window/level of emission from ICG in the NIR channel in each image and stack both DAPI and ICG channels into a single composite RGB image.

To calculate the average NIR emission intensity per cell ($\bar{I}_{cell}$) after incubation with μNETs or C^+-μNETs for durations of 30, 60, and 120 min, we summed the NIR intensity values for

all pixels in a given image, divided the total intensity by the number of cells in the image, and finally averaged among four images of the same batch of cells as follows

$$\bar{I}_{\text{cell}} = \frac{1}{4}\sum_{n=1}^{4} \frac{\sum_{x=1}^{512}\sum_{y=1}^{512} I(x,y)}{n_{\text{cells}}} \quad (4)$$

where $I(x, y)$ is the NIR emission intensity value at the pixel position (x, y) in a given image and n_{cells} is the number of cells in the image, obtained by counting the number of the cell nuclei in the DAPI channel using ImageJ.[55]

In Vivo Assessment of μNET and C$^+$-μNET Biodistribution in Swiss Webster Mice.

Healthy female Swiss Webster (SW) mice (~7–9 weeks old) were obtained from Taconic Biosciences. All animal studies were performed under a protocol approved by the University of California, Riverside Institutional Animal Care and Use Committee (protocol A-20200027). Animals were anesthetized by inhalation of 2% isoflurane gas in oxygen. All animals were tail-vein injected with 100 μL of either μNETs or C$^+$-μNETs while under anesthesia. Mice were euthanized by inhalation of compressed CO_2 gas at 4 or 24 h postinjection of the particles. A total of 16 mice were used in this study with 4 mice per sample type (μNETs or C$^+$-μNETs) per euthanasia time point (4 or 24 h postinjection). Following euthanasia, we collected ~500 μL of blood from the heart by cardiac puncture and extracted the liver, lungs, spleen (organs associated with the RES), and the kidneys for ICG content quantification.[56]

For measurement of ICG in blood samples, the blood was first weighed and then mixed with 1 mL of 5% sodium dodecyl sulfate (SDS) to lyse all cells and μNETs/C$^+$-μNETs, thereby releasing ICG. The samples were then incubated at 4 °C for 30 min, followed by centrifugation at 15,000*g* for 1 h at 4 °C. The supernatant was collected for fluorescence measurements. For organ analysis, samples were weighed and then incubated in 1 mL of 5% SDS for 30 min at room temperature (RT) in the dark. Next, the organs were homogenized using a tissue homogenizer (Omni TH 115, Omni International). We then added 3 mL of 5% SDS to the homogenate and incubated the samples for 30 min at RT in the dark. The crude homogenate was centrifuged at 14,000g for 45 min at 10 °C to separate the aqueous ICG-containing organ extract (supernatant). 1 mL of the supernatant was collected from each tube and used for ICG fluorescence recording. For both blood and homogenized organs, fluorescence emission in the range of 795–900 nm was recorded in response to 780 ± 2.5 nm photoexcitation using a Fluorolog-3 spectrofluorometer (Jobin Yvon Inc., Edison, NJ). We used Gaussian profiles to fit the spectral data points.

Analysis of ICG Content in Blood and Organs.

The concentration of ICG in each sample of organ/blood was estimated by comparing the spectrally integrated fluorescence emission of the sample in the range of 795–900 nm to a calibration curve that related the concentration of ICG dissolved in 5% SDS to the spectrally integrated emission of ICG in the same band and as measured by the Fluorolog-3 spectrofluorometer. We present the percentage of ICG recovered from each organ or blood

sample with respect to the initial injected dose per gram of organ. Statistical analysis of ICG content among various samples and time points was performed using a twotailed Student's *t*-test with equal variances.

RESULTS AND DISCUSSION

Characterizations.

Values of the ζ-potentials measured in 1× PBS were similar among RBCs (−14.07 ± 0.76 mV), μNETs (−14.84 ± 1.01 mV), and C $^{+}$-μNETs (−14.62 ± 0.71 mV). These results suggest that sialoglycoproteins, the primary negative charge-bearing components of the RBC membrane, were retained on μNETs and C^{+}-μNETs. Furthermore, these results also suggest that the presence of the hydrophilic hydroxyl group of cholesterol facing the external aqueous environment was insufficient to induce a statistically significant difference in the mean ζ potential of C^{+}-μNETs as compared to μNETs.

Illustrative absorption spectra of μNETs and C^{+}-μNETs associated with samples that were injected into mice are shown in Figure 2A. Absorption at 280 nm is attributed to the amino acids (e.g., tyrosine, tryptophan, phenylalanine, and histidine) associated with aromatic rings.[57,58] We observed that the absorbance value at 280 nm was nearly the same for μNETs and C^{+}-μNETs, suggesting that both samples contained approximately the same number of particles.

Absorption peaks at 412, 541, and 576 nm are the respective Soret peak and fundamental band (Q_0) and its vibronic tone (Q_v) for porphyrin $\pi \rightarrow \pi^*$ transitions associated with oxyhemoglobin. The higher absorbance values at these wavelengths for C^{+}-μNETs (compared to μNETs) indicates greater hemoglobin content in these particles. This is likely due to increased stability of the cholesterol-enriched RBC membrane during hypotonic treatment. Cholesterol is known to affect protein–protein interactions at the band 3 complex, which forms linkages with the underlying cytoskeletal network.[59,60] The increased presence of cholesterol may serve to stabilize the RBC membrane and reduce the amount of hemoglobin lost during hypotonic treatment of the cholesterol-enriched RBCs.

Samples of μNETs and C^{+}-μNETs exhibited similar fluorescence emission characteristics as quantified by the normalized fluorescence intensities (Figure 2B) and the spectrally integrated emission intensities (Figure 2C). These results indicate that membrane cholesterol enrichment did not significantly alter the emission characteristics of the particles. We suggest that ICG and cholesterol either did not colocalize in the same membrane domains to allow interactions that may have altered the emission characteristics of ICG or if they colocalized, the ICG emission characteristics were not altered due to interactions with cholesterol. Our findings are consistent with a previous study where the emission of free ICG in aqueous solution containing cholesterol was not altered.[61]

Reduced Externalization of PS on μNETs via Membrane Cholesterol Enrichment.

There was a small (~12%), but statistically significant ($p < 0.05$), reduction in the membrane cholesterol content of μNETs as compared to RBCs (Figure 3A). A possible reason for this relatively small reduction is that the lower numbers of particles may have been assayed

in the μNET sample as compared to RBCs while performing the cholesterol quantification assay. There was nearly a sixfold increase in membrane cholesterol content of C^+-μNETs as compared to RBCs ($p < 0.001$) (Figure 3A), indicating a large capacity for enrichment of the membrane with cholesterol. We found that a concentration of 15 mM cholesterol in the cholesterol—MβCD solution was sufficient to saturate the membranes (Figure S1).

As evidenced by the flow cytometry results, the ΔMFI associated with AF488-labeled annexin V for μNETs was about 1000 times higher than that of RBCs ($p < 0.01$) (Figure 3B), indicating that μNETs had higher levels of PS externalization. Membrane cholesterol enrichment resulted in approximately ~26-fold reduction in ΔMFI for C^+-μNETs as compared to that of μNETs ($p < 0.01$) (Figure 3B), indicating the effectiveness of cholesterol in lowering PS externalization, albeit not to the level associated with RBCs.

Values of SSC-A, which are proportional to the intracellular content of the cells or particles, were highest for RBCs as compared to those of μNETs and C^+-μNETs (Figure 3C), consistent with highest level of hemoglobin in RBCs. Similarly, minimal fluorescence emission due to PS surface expression was detected from RBCs. In general, μNETs exhibited the lowest values of SSC-A and fluorescence emission, indicative of their least amount of hemoglobin and highest PS externalization. The range of SSC-A values for C^+-μNETs was higher than the range for μNETs, consistent with the higher residual hemoglobin in these particles as compared to μNETs (Figure 2A), but lower than the range for RBCs, indicative of the lower hemoglobin content in C^+-μNETs. The variation in SSC-A for C^+-μNETs can be attributed to intraparticle differences in the hemoglobin and ICG content of these particles. We assume the addition of membrane cholesterol competes with the depletion of the hemoglobin process during the hypotonic treatment,[62] resulting in a mixture of microsized particles with different degrees of depleted hemoglobin level.

C^+-μNETs exhibited a relatively broad range for PS fluorescence (Figure 3C), suggesting that there was a nonuniformity in membrane cholesterol enrichment, which resulted in a nonhomogeneous population of C^+-μNETs with varying degrees of PS externalization. Because the lower bound of the SSC-A value for C^+-μNETs was associated with particles with various levels of cholesterol, it appears that cholesterol enrichment does not make a significant contribution to the SSC-A values for C^+-μNETs. The number–count plot of particles as determined by flow cytometry provided further evidence that there were C^+-μNETs with various degrees of PS externalization (Figure 3D). We considered all particles with PS labeling greater than 10^2 to be PS positive. Based on this threshold, only 0.11% of RBCs were PS positive, whereas ~99% of μNETs were PS positive (Figure 3E). The cholesterol-enriched C^+-μNETs had a significantly lower PS positivity fraction of ~40% (i.e., less than half as compared to μNETs).

Morphological Characteristics of Cholesterol-Enriched μNETs.

While the SSC-A data provide information about the intracellular components, we also present the FSC-A data as an indication of the size of RBCs and the microparticles (Figure 4A). As expected, RBCs had the greatest FSC-A and SSC-A[63,64] due to their relatively large size and presence of hemoglobin and other intracellular components. μNETs, however, had the lowest FSC-A values (Figure 4A), indicating their smallest size as compared to RBCs

and C^+-μNETs, with the latter having intermediate values of FSC-A. Our analysis based on QPI indicated that the respective mean ± SD diameters of RBCs, μNETs, and C^+-μNETs were 8.3 ± 0.6, 6.7 ± 0.9, and 7.1 ± 0.7 μm (Figure 4B–D).

Using QPI, we could detect the normal biconcave discoid shape of RBCs (Figure 4B, red arrows). We also detected echinocytes (Figure 4B, blue arrows) and acanthocytes (Figure 4B, black arrows) among the RBC population.

QPI of μNETs illustrated that these particles had a brighter rim (Figure 4C, purple arrows), evidenced by higher phase values, as compared to the central part of the particles, indicative of the localization of the residual hemoglobin near the membrane. Spatial variations in the phase values suggest the variabilities in hemoglobin localization and content among the μNETs. The near-zero phase values in the center of μNETs confirm our spectroscopic findings that μNETs contained minimal hemoglobin.

Based on QPI, we observed two distinct subpopulations of C^+-μNETs (Figure 4D), consistent with the corresponding SSC-A versus FSC-A plots for these particles (Figure 4A). The subpopulation with lower FSC-A and SSC-A values was more similar to μNETs with corresponding phase shifts and morphology (Figure 4D, purple arrows). The other subpopulation appeared similar to RBCs (Figure 4D, red arrows) with higher FSC-A and SSC-A values, a biconcave discoid shape, central dimple, and large phase shifts due to increased hemoglobin content (Figure 4D, red arrows).

Cholesterol-Enriched NETs Show Reduced Uptake by RAW 264.7 Macrophages.

Illustrative NIR fluorescence images of RAW 264.7 cells after 30–120 min of incubation with μNETs or C^+-μNETs are shown in Figure 5A. We observed higher NIR emission at 60 and 120 min from the cells incubated with μNETs, indicating that phagocytosis of μNETs occurred at a more rapid rate than phagocytosis of C^+-μNETs, resulting in greater uptake of μNETs at these time points.

At the 30 min time point, there was not a statistically significant difference in the mean fluorescence intensity of RAW 264.7 macrophages incubated with either μNETs or C^+-μNETs (Figure 5B). After 60 and 120 min of incubation, cells incubated with C^+-μNETs showed significantly lower mean fluorescence intensity compared to cells incubated with μNETs (Figure 5B). There was not a statistically significant difference between the mean fluorescence intensity of cells at 30 or 60 min of incubation with C^+-μNETs ($p > 0.1$); however, at 120 min of incubation with C^+-μNETs, the mean intensity became significantly larger as compared to the value at 60 min ($p = 0.03$). In comparison, the mean fluorescence intensity for cells incubated with μNETs continued to statistically increase from 30 to 120 min. These results indicate that membrane cholesterol enrichment was effective in delaying the phagocytosis of C^+-μNETs due to their reduced PS externalization as compared to μNETs.

In-Vivo Biodistribution.

To evaluate the efficacy of cholesterol enrichment on prolonging the circulation of μNETs, we analyzed the biodistribution of μNETs and C^+-μNETs in healthy SW mice. We recorded

fluorescence emission spectra (795–900 nm emission in response to 780 nm excitation) of blood and organs (liver, spleen, lungs, and kidneys) extracted from mice at 4 and 24 h following tail-vein injection of μNETs or C^+-μNETs. The liver, spleen, and lungs are the primary organs of the RES with an abundance of phagocytic cells that uptake foreign materials.[65] The spleen is a blood filtration organ equipped with macrophages that recognize and uptake senescent RBCs expressing PS on their outer leaflets. The liver contains Kupffer cells, which are adherent macrophages on the endothelial lining of the liver sinusoids. The lungs also have a large population of alveolar macrophages that are capable of engulfing microparticles, as well as a dense network of capillaries that can effectively trap exogenous particles.[66]

At 4 h postinjection, the Gaussian fits to the fluorescence emission intensity spectrum of blood from mice injected with μNETs were lower than that of mice injected with C^+-μNETs (Figure 6A). A similar trend was observed at 24 h postinjection. These results indicate that C^+-μNETs remained in the blood circulation longer than μNETs for at least up to 24 h after intravascular injection.

As a metric for quantifying μNET and C^+-μNET fluorescence in the blood and organs, we used the value of the integrated NIR fluorescence emission across 795–900 nm normalized by the mass of the organ/blood. We observed that the fluorescence signal per gram of extracted blood for C^+-μNETs was significantly greater than that of μNETs at both 4 and 24 h time points (~69 and 182% greater, respectively) (Figure 6B). Between these time points, the mass-normalized integrated fluorescence signal of μNETs in blood decreased by ~ 62%, while that of C^+-μNETs only decreased by about 37%, indicating prolonged circulation of C^+-μNETs compared to μNETs.

Analysis of the liver, lungs, kidneys, and spleen revealed that the mass-normalized integrated fluorescence of μNETs was significantly higher in these organs as compared to that of C^+-μNETs at 4 h (Figure 6B). These results suggest that the prolonged circulation time of C^+-μNETs over the first few hours following tail-vein injection is concomitant with reduced accumulation of C^+-μNETs in the RES organs and kidneys. At 24 h, the mass-normalized integrated fluorescence of C^+-μNETs was significantly higher than that of μNETs in the lungs (also in the liver and spleen, but not significantly). These results are ostensibly due to clearance of the rapidly sequestered μNETs from these organs via alveolar, hepatic, and splenic phagocytosis pathways and the delayed accumulation of C^+-μNETs in these organs over 24 h.

We also quantified the biodistribution of particles in the blood and the extracted organs by calculating the percent of the injected dose (ID) recovered in the organ, normalized by the organ mass (% ID/g) (Figure 6C). The mass-normalized fraction of the initial dose of C^+-μNETs in the blood was significantly higher than that of μNETs at 4 h (~74 vs 49% ID/g; 1.5-fold increase) and 24 h (~63 vs 35% ID/g; 1.8-fold increase), indicating that the reduced PS externalization due to membrane cholesterol enrichment was effective in prolonging the circulation time of C^+-μNETs compared to μNETs.

Hepatic removal of RBCs has been shown to positively correlate with the amount of externalized PS.[67] Consistent with this previous study, we found that for C^+-μNETs only about 7.5% ID/g had accumulated in the liver as compared to 17.2% ID/g for μNETs at 4 h postinjection ($p < 0.01$) (Figure 6C). Similarly, at the 4 h time point, the mass-normalized fraction of μNETs in the spleen (~7.1% ID/g) was significantly higher than fraction of C^+-μNETs (~4.4% ID/g) ($p < 0.001$) (Figure 6C), indicating the higher uptake of μNETs by the splenic macrophages. We attribute the greater accumulation of μNETs in the liver and spleen at 4 h to the greater degree of externalized PS on the surface of μNETs, causing them to be more readily recognized and engulfed by hepatocytes, and Kupffer cells[68,69] and splenic macrophages. At 24 h, the hepatic fraction of μNETs significantly decreased to ~2.6% ID/g (Figure 6C and Table S1), indicating clearance via the hepatobiliary mechanism. At this time point, the hepatic fraction of C^+-μNETs increased to ~4.5% ID/g (Figure 6C and Table S1), indicating their slower rate of accumulation in the liver.

We also compared the recovered mass-normalized fractions of μNETs and C^+-μNETs between the various organs (Table S2). At the 4 h time point, the liver was the primary site of accumulation for both μNETs and C^+-μNETs. The exception was the lungs where the amount of C^+-μNETs was not significantly different from the liver. At 24 h, the primary sites of accumulation for both μNETs and C^+-μNETs were the lungs and spleen.

The total recovered mass-normalized percentages of μNETs and C^+-μNETs recovered from the blood, liver, lungs, kidneys, and spleen were ~87 and 96% ID/g at 4 h, respectively. At 24 h, the recovered fraction of μNETs was reduced to ~57% ID/g, whereas ~94% ID/g of C^+-μNETs was recovered from these compartments. The relatively high recovery of C^+-μNETs at 24 h indicates minimal hepatobiliary elimination, phagocytic removal, or urinary excretion of these particles, whereas nearly half of the initial dose per gram of organs for μNETs was eliminated from these compartments by that time.

CONCLUSIONS

Externalization of PS on the surface of RBC-derived particles, such as μNETs, can be reduced by membrane cholesterol enrichment. Our in-vitro results indicate that uptake of cholesterol-enriched μNETs (C^+-μNETs) by RAW 264.7 murine macrophages takes place at a lowered rate as compared to μNETs without cholesterol enrichment. When administered intravenously via tail-vein injection in healthy mice, the % ID/g of C^+-μNETs in blood at 4 and 24 h was ~1.5 and 1.8 times higher than that of μNETs. At 4 h postinjection, μNETs and C^+-μNETs that were removed from circulation had primarily accumulated in the liver with lungs as an additional accumulation site for C^+-μNETs. At 24 h postinjection, the % ID/g of μNETs and C^+-μNETs was greatest in blood, followed by the lungs and spleen. The total mass-normalized percentage of the initial C^+-μNETs dose at 24 h was 94% ID/g, but only 57% ID/g for μNETs. These results indicate that membrane cholesterol enrichment is an effective method to reduce PS externalization on the surface of RBC-derived particles and can prolong their circulation in the blood.

Supplementary Material

Refer to Web version on PubMed Central for supplementary material.

ACKNOWLEDGMENTS

This study was supported in part by a grant from the National Institute of Arthritis and Musculoskeletal and Skin Diseases (R01-AR068067). We thank the University of California Leadership Excellence through Advanced DegreeS (UC LEADS) program for enabling author C.A. to contribute to the experiments and analysis involving the in-vitro uptake of the particles by the macrophages presented in this manuscript.

ABBREVIATIONS

AF488	Alexa Fluor 488
C^+-μNETs	cholesterol-enriched μNETs
FSC-A	forward scattering area
ICG	indocyanine green
ID	injected dose
MβCD	methyl-β-cyclodextrin
NETs	NIR erythrocyte-derived transducers
NIR	near infrared
PBS	phosphate-buffered saline
PC	phosphatidylcholine
PE	phosphatidylethanolamine
PS	phosphatidylserine
RBCs	red blood cells
RES	reticuloendothelial system
SDS	sodium dodecyl sulfate
SLM	spatial light modulator
SM	sphingomyelin
SSC-A	side scattering area
SW	Swiss Webster
QPI	quantitative phase imaging
μNETs	microsized NIR erythrocyte-derived transducers

REFERENCES

(1). Villa CH; Anselmo AC; Mitragotri S; Muzykantov V Red Blood Cells: Supercarriers for Drugs, Biologicals, and Nanoparticles and Inspiration for Advanced Delivery Systems. Adv. Drug Delivery Rev 2016, 106, 88–103.

(2). Zhao Z; Ukidve A; Gao Y; Kim J; Mitragotri S Erythrocyte Leveraged Chemotherapy (ELeCt): Nanoparticle Assembly on Erythrocyte Surface to Combat Lung Metastasis. Sci. Adv 2019, 5, No. eaax9250. [PubMed: 31763454]

(3). Gao M; Hu A; Sun X; Wang C; Dong Z; Feng L; Liu Z Photosensitizer Decorated Red Blood Cells as an Ultrasensitive Light Responsive Drug Delivery System. ACS Appl. Mater. Interfaces 2017, 9, 5855–5863. [PubMed: 28117965]

(4). Luo L; Zeng F; Xie J; Fan J; Xiao S; Wang Z; Xie H; Liu B A RBC Membrane-Camouflaged Biomimetic Nanoplatform for Enhanced Chemo-Photothermal Therapy of Cervical Cancer. J. Mater. Chem. B 2020, 8, 4080–4092. [PubMed: 32239064]

(5). Burns JM; Vankayala R; Mac JT; Anvari B Erythrocyte-Derived Theranostic Nanoplatforms for Near Infrared Fluorescence Imaging and Photodestruction of Tumors. ACS Appl. Mater. Interfaces 2018, 10, 27621–27630. [PubMed: 30036031]

(6). Sternberg N; Georgieva R; Duft K; Bäumler H Surface-Modified Loaded Human Red Blood Cells for Targeting and Delivery of Drugs. J. Microencapsulation 2012, 29, 9–20. [PubMed: 22034952]

(7). Bahmani B; Bacon D; Anvari B Erythrocyte-Derived Photo-Theranostic Agents: Hybrid Nano-Vesicles Containing Indocyanine Green for Near Infrared Imaging and Therapeutic Applications. Sci. Rep 2013, 3, 2180. [PubMed: 23846447]

(8). Aryal S; Nguyen TDT; Pitchaimani A; Shrestha TB; Biller D; Troyer D Membrane Fusion-Mediated Gold Nanoplating of Red Blood Cell: A Bioengineered CT-Contrast Agent. ACS Biomater. Sci. Eng 2017, 3, 36–41. [PubMed: 33429682]

(9). Hanley T; Vankayala R; Lee C-H; Tang JC; Burns JM; Anvari B Phototheranostics Using Erythrocyte-Based Particles. Biomolecules 2021, 11, 729. [PubMed: 34068081]

(10). Han X; Wang C; Liu Z Red Blood Cells as Smart Delivery Systems. Bioconjugate Chem. 2018, 29, 852–860.

(11). Millán CG; Marinero MLS; Castañeda AZ; Lanao JM Drug, Enzyme and Peptide Delivery using Erythrocytes as Carriers. J. Controlled Release 2004, 95, 27–49.

(12). Wang P; Wang X; Luo Q; Li Y; Lin X; Fan L; Zhang Y; Liu J; Liu X Fabrication of Red Blood Cell-Based Multimodal Theranostic Probes for Second Near-Infrared Window Fluorescence Imaging-Guided Tumor Surgery and Photodynamic Therapy. Theranostics 2019, 9, 369–380. [PubMed: 30809280]

(13). Rao L; Cai B; Bu L-L; Liao Q-Q; Guo S-S; Zhao X-Z; Dong W-F; Liu W Microfluidic Electroporation-Facilitated Synthesis of Erythrocyte Membrane-Coated Magnetic Nanoparticles for Enhanced Imaging-Guided Cancer Therapy. ACS Nano 2017, 11, 3496–3505. [PubMed: 28272874]

(14). López SCB; Meissner KE Characterization of Carrier Erythrocytes for Biosensing Applications. J. Biomed. Opt 2017, 22, 091510.

(15). Flower RW; Kling R Observation and Characterization of Microvascular Vasomotion using Erythrocyte Mediated ICG Angiography (EM-ICG-A). Microvasc. Res 2017, 113, 78–87. [PubMed: 28390895]

(16). Wang D; Haytham A; Mayo L; Tao Y; Saeedi O Automated Retinal Microvascular Velocimetry Based on Erythrocyte Mediated Angiography. Biomed. Opt. Express 2019, 10, 3681–3697. [PubMed: 31360609]

(17). van Meer G; Voelker DR; Feigenson GW Membrane Lipids: Where They Are and How They Behave. Nat. Rev. Mol. Cell Biol 2008, 9, 112–124. [PubMed: 18216768]

(18). Zachowski A Phospholipids in Animal Eukaryotic Membranes - Transverse Asymmetry and Movement. Biochem. J 1993, 294, 1–14. [PubMed: 8363559]

(19). Kodigepalli KM; Bowers K; Sharp A; Nanjundan M Roles and Regulation of Phospholipid Scramblases. FEBS Lett. 2015, 589, 3–14. [PubMed: 25479087]

(20). Jia W; Burns JM; Villantay B; Tang JC; Vankayala R; Lertsakdadet B; Choi B; Nelson JS; Anvari B Intravital Vascular Phototheranostics and Real-Time Circulation Dynamics of Micro- and Nanosized Erythrocyte-Derived Carriers. ACS Appl. Mater. Interfaces 2020, 12, 275–287. [PubMed: 31820920]

(21). Schwarz S; Deuticke B; Haest CWM Passive Transmembrane Redistributions of Phospholipids as a Determinant of Erythrocyte Shape Change. Studies on Electroporated Cells. Mol. Membr. Biol 1999, 16, 247–255. [PubMed: 10503246]

(22). Henszen MMM; Weske M; Schwarz S; Haest CWM; Deuticke B Electric Field Pulses Induce Reversible Shape Transformation of Human Erythrocytes. Mol. Membr. Biol 1997, 14, 195–204. [PubMed: 9491371]

(23). Haest CWM; Kamp D; Deuticke B Transbilayer Reorientation of Phospholipid Probes in the Human Erythrocyte Membrane. Lessons from Studies on Electroporated and Resealed Cells. Biochim. Biophys. Acta, Biomembr 1997, 1325, 17–33.

(24). Dressler V; Schwister K; Haest CWM; Deuticke B Dielectric-Breakdown of the Erythrocyte-Membrane Enhances Transbilayer Mobility of Phospholipids. Biochim. Biophys. Acta 1983, 732, 304–307. [PubMed: 6871195]

(25). Mambrini G; Mandolini M; Rossi L; Pierigè F; Capogrossi G; Salvati P; Serafini S; Benatti L; Magnani M Ex Vivo Encapsulation of Dexamethasone Sodium Phosphate into Human Autologous Erythrocytes using Fully Automated Biomedical Equipment. Int. J. Pharm 2017, 517, 175–184. [PubMed: 27939571]

(26). Devitt A; Moffatt OD; Raykundalia C; Capra JD; Simmons DL; Gregory CD Human CD14 Mediates Recognition and Phagocytosis of Apoptotic Cells. Nature 1998, 392, 505–509. [PubMed: 9548256]

(27). Zwaal RFA; Comfurius P; Bevers EM Surface Exposure of Phosphatidylserine in Pathological Cells. Cell. Mol. Life Sci 2005, 62, 971–988. [PubMed: 15761668]

(28). Arashiki N; Saito M; Koshino I; Kamata K; Hale J; Mohandas N; Manno S; Takakuwa Y An Unrecognized Function of Cholesterol: Regulating the Mechanism Controlling Membrane Phospholipid Asymmetry. Biochemistry 2016, 55, 3504–3513. [PubMed: 27267274]

(29). Zhou Q; Zhao J; Stout JG; Luhm RA; Wiedmer T; Sims PJ Molecular Cloning of Human Plasma Membrane Phospholipid Scramblase. A Protein Mediating Transbilayer Movement of Plasma Membrane Phospholipids. J. Biol. Chem 1997, 272, 18240–18244. [PubMed: 9218461]

(30). van Zwieten R; Bochem AE; Hilarius PM; van Bruggen R; Bergkamp F; Hovingh GK; Verhoeven AJ The Cholesterol Content of the Erythrocyte Membrane is an Important Determinant of Phosphatidylserine Exposure. Biochim. Biophys. Acta, Mol. Cell Biol. Lipids 2012, 1821, 1493–1500.

(31). Posada IMD; Fantini J; Contreras FX; Barrantes F; Alonso A; Goñi FM A Cholesterol Recognition Motif in Human Phospholipid Scramblase 1. Biophys. J 2014, 107, 1383–1392. [PubMed: 25229146]

(32). Hoekstra LT; de Graaf W; Nibourg GAA; Heger M; Bennink RJ; Stieger B; van Gulik TM Physiological and Biochemical Basis of Clinical Liver Function Tests A Review. Ann. Surg 2013, 257, 27–36. [PubMed: 22836216]

(33). Yannuzzi LA Indocyanine Green Angiography: A Perspective on Use in the Clinical Setting. Am. J. Ophthalmol 2011, 151, 745–751. [PubMed: 21501704]

(34). Maarek J-MI; Holschneider DP; Harimoto J; Yang J; Scremin OU; Rubinstein EH Measurement of Cardiac Output with Indocyanine Green Transcutaneous Fluorescence Dilution Technique. Anesthesiology 2004, 100, 1476–1483. [PubMed: 15166567]

(35). Kim T; O'Brien C; Choi HS; Jeong MY Fluorescence Molecular Imaging Systems for Intraoperative Image-Guided Surgery. Appl. Spectrosc. Rev 2018, 53, 349–359.

(36). DSouza AV; Lin H; Henderson ER; Samkoe KS; Pogue BW Review of Fluorescence Guided Surgery Systems: Identification of Key Performance Capabilities Beyond Indocyanine Green Imaging. J. Biomed. Opt 2016, 21, 080901. [PubMed: 27533438]

(37). Boni L; David G; Mangano A; Dionigi G; Rausei S; Spampatti S; Cassinotti E; Fingerhut A Clinical Applications of Indocyanine Green (ICG) Enhanced Fluorescence in Laparoscopic Surgery. Surg. Endosc 2015, 29, 2046–2055. [PubMed: 25303914]

(38). Griffiths M; Chae MP; Rozen WM Indocyanine Green-Based Fluorescent Angiography in Breast Reconstruction. Gland Surg. 2016, 5, 133–149. [PubMed: 27047782]

(39). Nowak K; Karampinis I; Gerken ALH Application of Fluorescent Dyes in Visceral Surgery: State of the Art and Future Perspectives. Visc. Med 2020, 36, 80–87. [PubMed: 32355664]

(40). Burns JM; Shafer E; Vankayala R; Kundra V; Anvari B Near Infrared Fluorescence Imaging of Intraperitoneal Ovarian Tumors in Mice Using Erythrocyte-Derived Optical Nanoparticles and Spatially-Modulated Illumination. Cancers 2021, 13, 2544. [PubMed: 34067308]

(41). Koleva L; Bovt E; Ataullakhanov F; Sinauridze E Erythrocytes as Carriers: From Drug Delivery to Biosensors. Pharmaceutics 2020, 12, 276. [PubMed: 32197542]

(42). Bax BE Erythrocytes as Carriers of Therapeutic Enzymes. Pharmaceutics 2020, 12, 435. [PubMed: 32397259]

(43). Zidovetzki R; Levitan I Use of Cyclodextrins to Manipulate Plasma Membrane Cholesterol Content: Evidence, Misconceptions and Control Strategies. Biochim. Biophys. Acta, Biomembr 2007, 1768, 1311–1324.

(44). Slayden A; North K; Bisen S; Dopico AM; Bukiya AN; Rosenhouse-Dantsker A Enrichment of Mammalian Tissues and Xenopus Oocytes with Cholesterol. J. Visualized Exp 2020, 157, No. e60734.

(45). Tang JC; Partono A; Anvari B Near-Infrared-Fluorescent Erythrocyte-Mimicking Particles: Physical and Optical Characteristics. IEEE Trans. Biomed. Eng 2019, 66, 1034–1044. [PubMed: 30130175]

(46). Sarshar M; Lu T; Anvari B Combined Optical Micromanipulation and Interferometric Topography (COMMIT). Biomed. Opt. Express 2016, 7, 1365–1374. [PubMed: 27446661]

(47). Lu T; Anvari B Characterization of the Viscoelastic Properties of Ovarian Cancer Cells Membranes by Optical Tweezers and Quantitative Phase Imaging. Front. Phys 2020, 8, 582956.

(48). Burns JM; Saager R; Majaron B; Jia W; Anvari B Optical Properties of Biomimetic Probes Engineered from Erythrocytes. Nanotechnology 2017, 28, 035101. [PubMed: 27966473]

(49). Vankayala R; Mac JT; Burns JM; Dunn E; Carroll S; Bahena EM; Patel DK; Griffey S; Anvari B Biodistribution and Toxicological Evaluation of Micron- and Nano-Sized Erythrocyte-Derived Optical Particles in Healthy Swiss Webster Mice. Biomater. Sci 2019, 7, 2123–2133. [PubMed: 30869663]

(50). Tang JC; Vankayala R; Mac JT; Anvari B RBC-Derived Optical Nanoparticles Remain Stable After a Freeze-Thaw Cycle. Langmuir 2020, 36, 10003–10011. [PubMed: 32787036]

(51). Vrielink A; Ghisla S Cholesterol Oxidase: Biochemistry and Structural Features. FEBS J. 2009, 276, 6826–6843. [PubMed: 19843169]

(52). Jemaà M; Fezai M; Bissinger R; Lang F Methods Employed in Cytofluorometric Assessment of Eryptosis, the Suicidal Erythrocyte Death. Cell. Physiol. Biochem 2017, 43, 431–444. [PubMed: 28922657]

(53). Kuypers F; Lewis R; Hua M; Schott M; Discher D; Ernst J; Lubin B Detection of Altered Membrane Phospholipid Asymmetry in Subpopulations of Human Red Blood Cells using Fluorescently Labeled Annexin V. Blood 1996, 87, 1179–1187. [PubMed: 8562945]

(54). Taciak B; Białasek M; Braniewska A; Sas Z; Sawicka P; Kiraga Ł; Rygiel T; Król M; Evaluation of Phenotypic and Functional Stability of RAW 264.7 Cell Line through Serial Passages. PLoS One 2018, 13, No. e0198943. [PubMed: 29889899]

(55). Schneider CA; Rasband WS; Eliceiri KW NIH Image to ImageJ: 25 Years of Image Analysis. Nat. Methods 2012, 9, 671–675. [PubMed: 22930834]

(56). Wilhelm S; Tavares AJ; Dai Q; Ohta S; Audet J; Dvorak HF; Chan WCW Analysis of Nanoparticle Delivery to Tumours. Nat. Rev. Mater 2016, 1, 16014.

(57). Layne E. Spectrophotometric and Turbidimetric Methods for Measuring Proteins. Methods Enzymol. 1957, 3, 447–454.

(58). Stoscheck CM Quantitation of Protein. Methods Enzymol. 1990, 182, 50–68. [PubMed: 2314256]

(59). de Meyer FJ-M; Rodgers JM; Willems TF; Smit B Molecular Simulation of the Effect of Cholesterol on Lipid-Mediated Protein-Protein Interactions. Biophys. J 2010, 99, 3629–3638. [PubMed: 21112287]

(60). Pajic-Lijakovic I Erythrocytes Under Osmotic Stress - Modeling Considerations. Prog. Biophys. Mol. Biol 2015, 117, 113–124. [PubMed: 25433233]

(61). Yoneya S; Saito T; Komatsu Y; Koyama I; Takahashi K; Duvoll-Young J Binding Properties of Indocyanine Green in Human Blood. Invest. Ophthalmol. Visual Sci 1998, 39, 1286–1290. [PubMed: 9620093]

(62). Forsyth AM; Braunmuller S; Wan J; Franke T; Stone HA The Effects of Membrane Cholesterol and Simvastatin on Red Blood Cell Deformability and ATP Release. Microvasc. Res 2012, 83, 347–351. [PubMed: 22349292]

(63). Ensinck MA; Brajovich MEL; Borrás SEG; Cotorruelo CM; Biondi CS Erythrocyte Senescent Markers by Flow Cytometry. Open J. Blood Dis 2019, 09, 47–59.

(64). Canellini G; Rubin O; Delobel J; Crettaz D; Lion N; Tissot JD Red Blood Cell Microparticles and Blood Group Antigens: An Analysis by Flow Cytometry. Blood Transfus. 2012, 10, s39–s45. [PubMed: 22890266]

(65). Alric C; Miladi I; Kryza D; Taleb J; Lux F; Bazzi R; Billotey C; Janier M; Perriat P; Roux S; Tillement O The Biodistribution of Gold Nanoparticles Designed for Renal Clearance. Nanoscale 2013, 5, 5930–5939. [PubMed: 23702968]

(66). Blanco E; Shen H; Ferrari M Principles of Nanoparticle Design for Overcoming Biological Barriers to Drug Delivery. Nat. Biotechnol 2015, 33, 941–951. [PubMed: 26348965]

(67). Schroit AJ; Madsen JW; Tanaka Y In Vivo Recognition and Clearance of Red Blood Cells Containing Phosphatidylserine in their Plasma Membranes. J. Biol. Chem 1985, 260, 5131–5138. [PubMed: 3988747]

(68). Lee S-J; Park S-Y; Jung M-Y; Bae SM; Kim I-S Mechanism for Phosphatidylserine-Dependent Erythrophagocytosis in Mouse Liver. Blood 2011, 117, 5215–5223. [PubMed: 21427291]

(69). Zhang Y-N; Poon W; Tavares AJ; McGilvray ID; Chan WCW Nanoparticle-Liver Interactions: Cellular Uptake and Hepatobiliary Elimination. J. Controlled Release 2016, 240, 332–348.

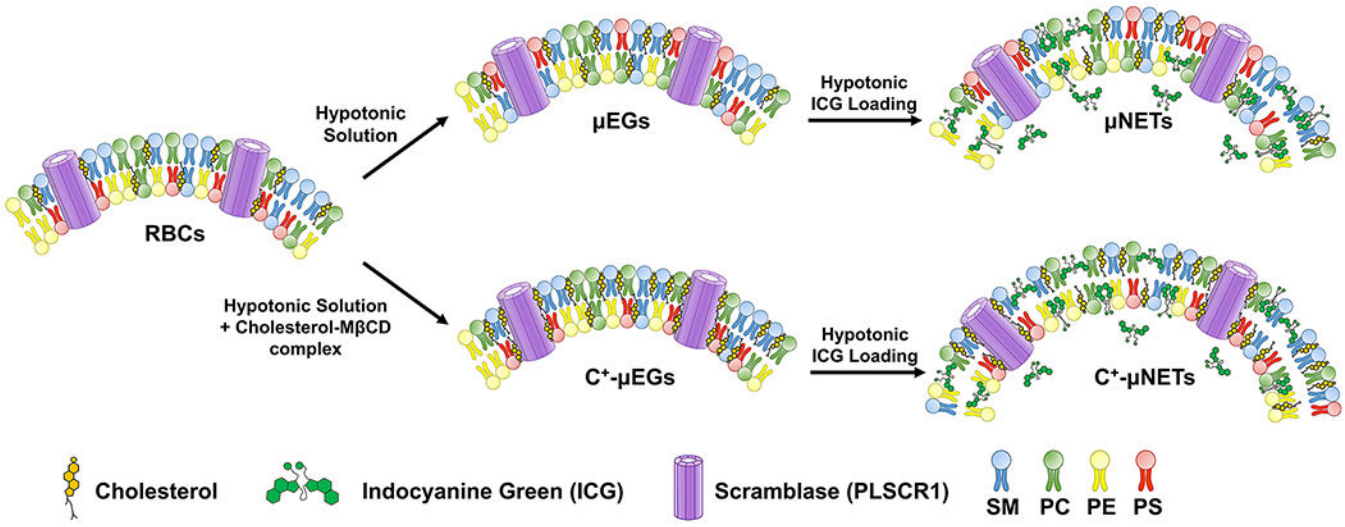

Figure 1.

Schematic of the methods to form μNETs and C^+-μNETs. For C^+-μNETs, the cholesterol–MβCD complex was added in a hypotonic solution during simultaneous hemoglobin depletion and membrane enrichment with cholesterol prior to ICG loading.

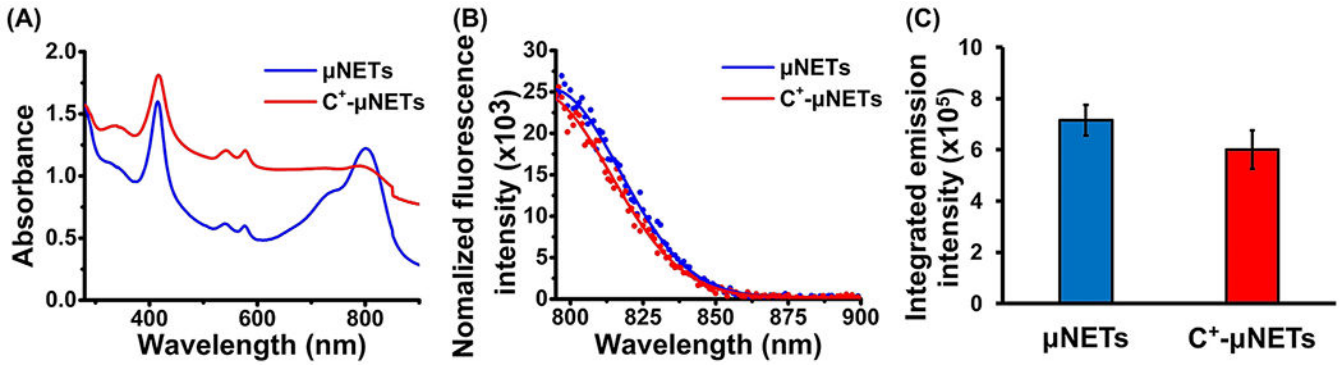

Figure 2.

Optical characteristics of μNETs and C^+-μNETs. (A) Absorption spectra corresponding to the average of three independent measurements for each sample. (B) Normalized fluorescence emission spectra in response to 780 ± 2.5 nm photoexcitation. Data points correspond to the average of three measurements. Solid traces are the Gaussian fits to the averaged data. (C) Emission intensities integrated over the 795–900 spectral band. Each bar is an average of three independent measurements with error bars representing the SDs (n = 3).

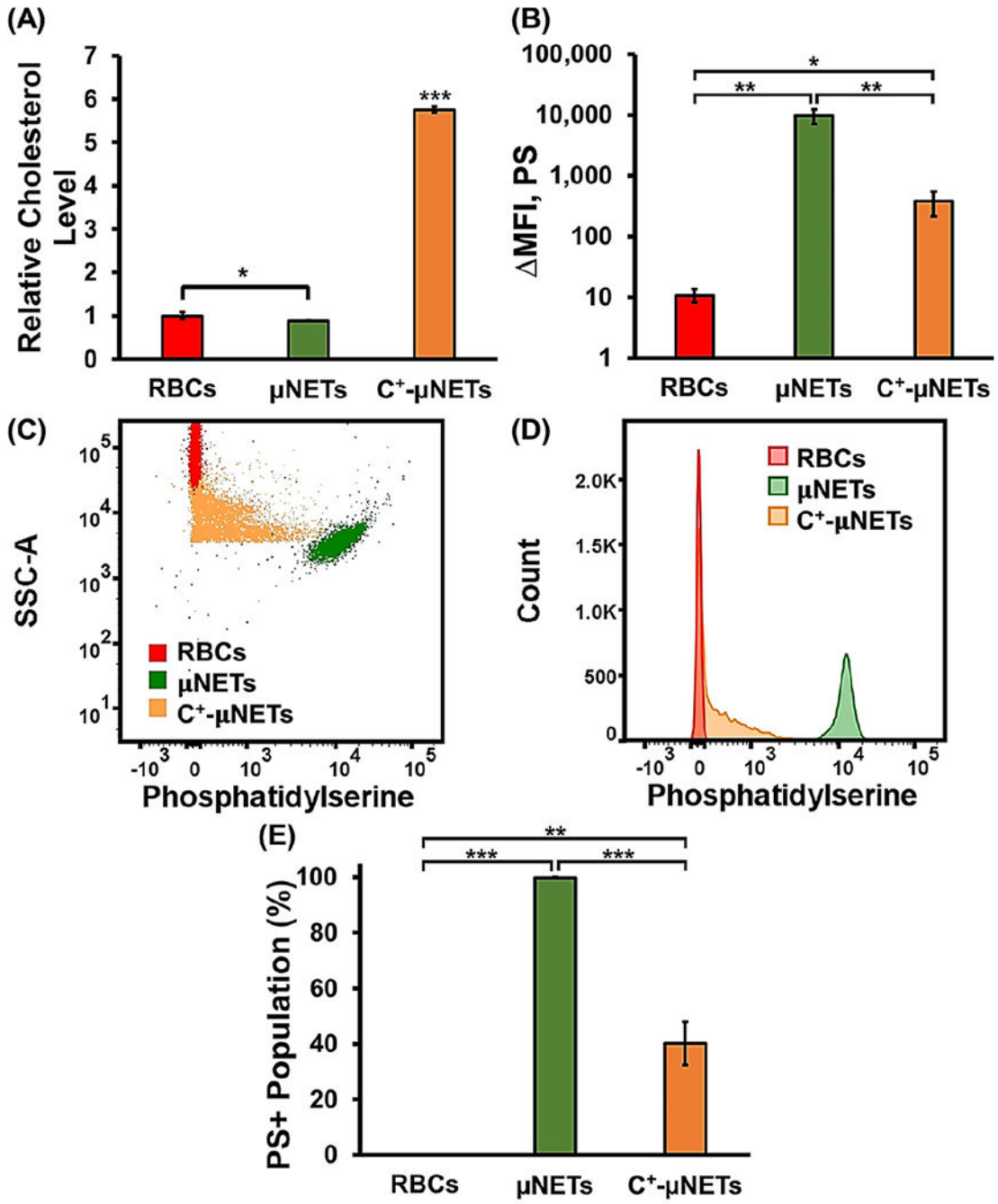

Figure 3.

Quantification of cholesterol content and detection of externalized PS. (A) Relative average membrane cholesterol level of RBCs, μNETs, and C$^+$-μNETs. Each bar is an average of four independent measurements ($n = 4$). (B) ΔMFI of RBCs, μNETs, and C$^+$-μNETs conjugated with AF488-labeled annexin V for PS detection. Each bar represents the average of three independent measurements. (C) Representative dot plots of SSC-A vs fluorescently detected PS for RBCs, μNETs, and C$^+$-μNETs. (D) Representative counts of RBCs, μNETs, and C$^+$-μNETs fluorescently detected for PS. (E) Mean fractions of PS-positive RBCs, μNETs,

and C^{+}-μNETs associated with three measurements. Error bars in panels (A,B,E) represent SDs. Asterisks *, **, and ***, respectively, correspond to statistically significant differences with $p < 0.05$, $p < 0.01$, and $p < 0.001$.

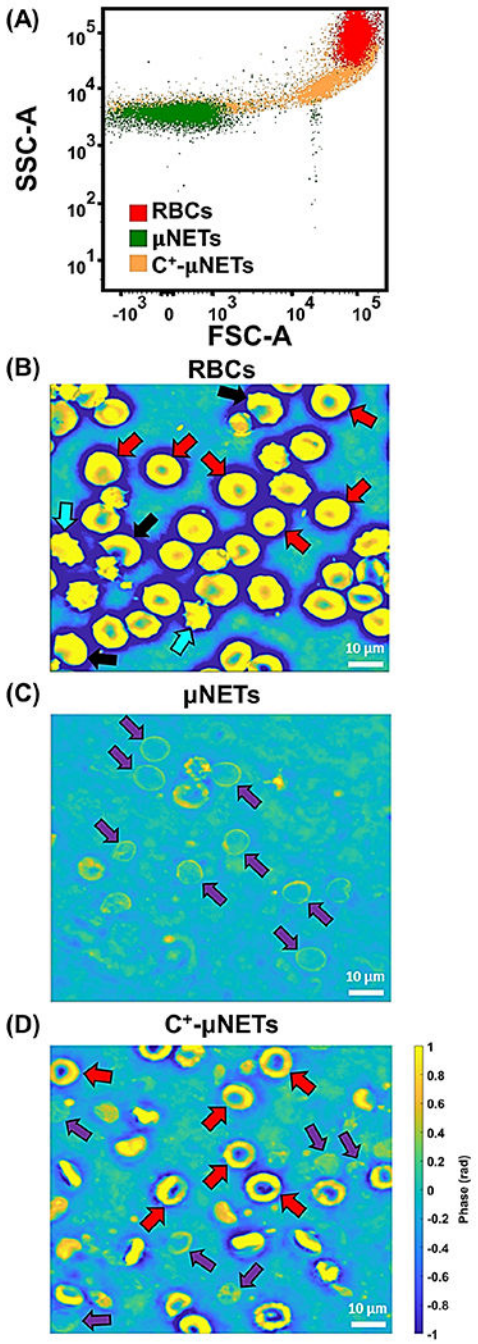

Figure 4.

Morphological characteristics of RBCs, μNETs, and C^+-μNETs. (A) Representative SSC-A vs FSC-A plots of RBCs, μNETs, and C^+-μNETs obtained by flow cytometry. Representative falsely colored images of (B) RBCs, (C) μNETs, and (D) C^+-μNETs obtained by QPI. In panel (B), examples of normal RBCs, echinocytes, and acanthocytes are pointed out by the red, blue, and black arrows, respectively. Purple arrows point to μNETs in panel (C). In panel (D), examples of C^+-μNETs resembling RBCs or μNETs are pointed out by the respective red and purple arrows. The scale bar for the phase values applies to panels (B–D).

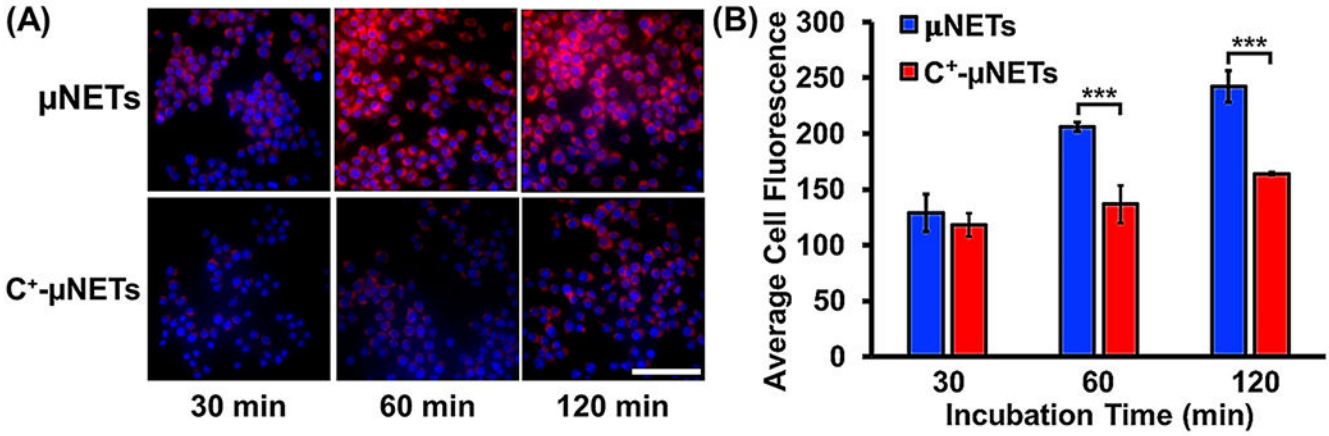

Figure 5.

In-vitro uptake dynamics of μNETs and C^+-μNETs by RAW 264.7 murine macrophages. (A) Fluorescence images of RAW 264.7 macrophages after 30, 60, and 120 min of incubation with μNETs or C^+-μNETs. Scale bar = 50 μm and applies to all panels. (B) Average NIR fluorescence intensity of RAW 264.7 cells (estimated using eq 4) after incubation with μNETs or C^+-μNETs for 30, 60, and 120 min. Error bars are the SDs, and statistical significance is denoted with *** asterisks indicating $p < 0.001$.

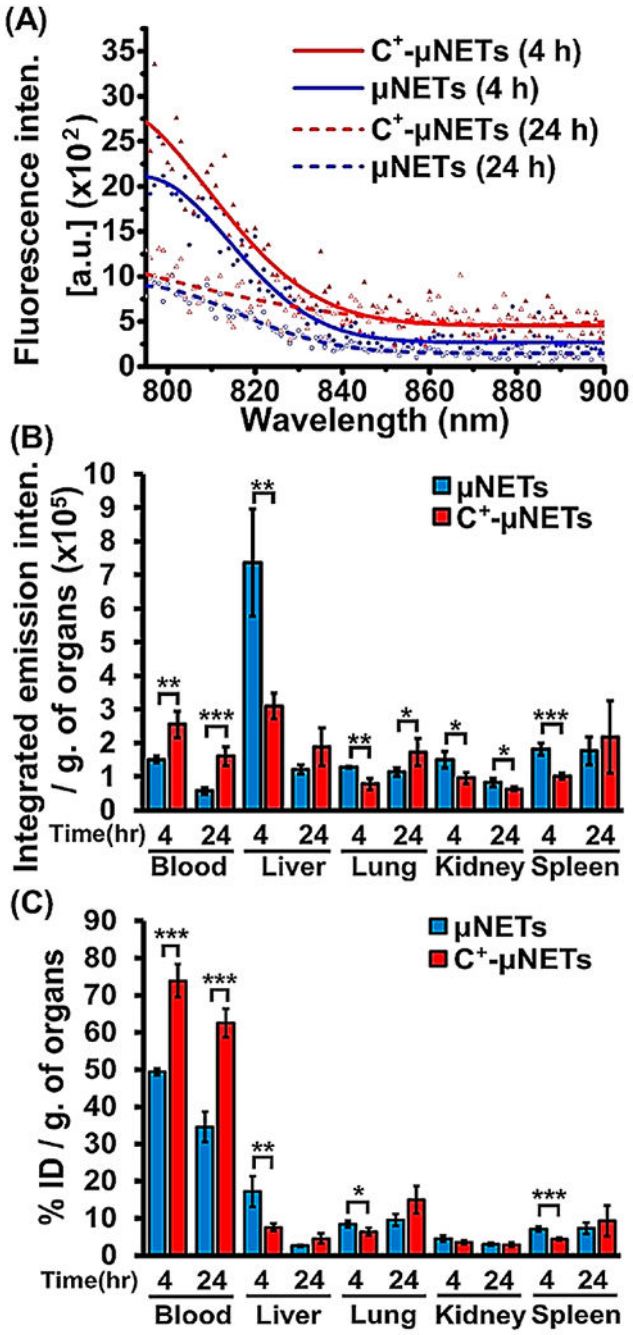

Figure 6.

Biodistribution of μNETs and C^+-μNETs. (A) Fluorescence emission spectra of blood collected from mice at 4 and 24 h following tail-vein injection of μNETs and C^+-μNETs in response to 780 ± 2.5 nm photoexcitation. Solid traces are Gaussian fits to the data points (C^+-μNETs at 4 h represented by filled triangles; μNETs at 4 h represented by filled circles; C^+-μNETs at 24 h represented by unfilled triangles; and μNETs at 24 h represented by unfilled circles). (B) Spectrally integrated emission intensity of blood and homogenized organs normalized to the mass of the organ/blood. (C) Recovered percentage of the initial

dose of ICG normalized to the mass of extracted organs and blood (% ID/g) at 4 and 24 h postinjection of μNETs and C^+-μNETs. In each panel, the means of four independent measurements are presented. Error bars correspond to their SDs from the mean. Asterisks denote statistically significant differences (*, $p < 0.05$; **, $p < 0.01$; ***, $p < 0.001$) between the indicated pairs.